Inorganic Chemistry

pubs.acs.org/IC

Article

Mixed Anion Semiconductor $In_8S_{2.82}Te_{6.18}(Te_2)_3$

Rebecca McClain, Craig C. Laing, Jiahong Shen, Christopher Wolverton, and Mercouri G. Kanatzidis*

Cite This: *Inorg. Chem.* 2022, 61, 9040−9046

Read Online

ACCESS | Metrics & More | Article Recommendations | Supporting Information

ABSTRACT: The new heteroanionic compound $In_8S_{2.82}Te_{6.18}(Te_2)_3$ crystallizes in the monoclinic space group $C2/c$ with lattice parameters a = 14.2940(6) Å, b = 14.3092(4) Å, c = 14.1552(6) Å, and β = 90.845(3)°. The three-dimensional (3D) framework of $In_8S_{2.82}Te_{6.18}(Te_2)_3$ is composed of a complex 3D network of corner-connected InQ_4 tetrahedra with three Te_2^{2-} dumbbell dimers per formula unit. The optical bandgap is 1.12(2) eV and the work function is 5.15(5) eV. First-principles electronic structure calculations using density functional theory (DFT) indicate that this material has potential as a p-type thermoelectric material as it is a narrow bandgap semiconductor, incorporates several heavy elements, and has multiple overlapping bands near the valence band maximum.

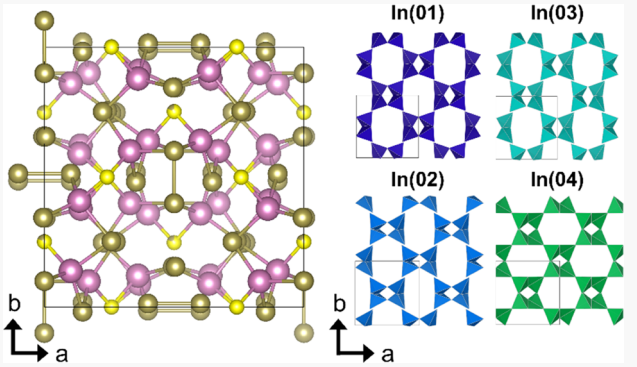

INTRODUCTION

The frontiers of modern chemistry and physics are advanced through the exploration of novel solid-state materials. Historically, the more complex compounds tend to have multiple cations and a single anion, which serve to create and control a variety of valuable properties. In contrast, heteroanionic materials are relatively underexplored due to their relative complexity and constitute an attractive chemical horizon to pursue in search of new materials.[1−6] Heteroanionic materials have multiple anions, each with its own crystallographically distinct site. The anionic diversity introduced to the material adds new dimensions of control and functionality, resulting from the different characteristics of the anions, such as charge, radii, electronegativity, and polarizability.[1,2] The introduction of these additional anions, as well as potential structural transformations that result, offers the opportunity to capitalize on structure−property relationships. This class of materials provides the potential to merge desirable properties from each single-anion component or even to produce advantageous properties unattainable through their single-anion predecessors.[1,6−8]

The difference in chemical nature of the anions in heteroanionic materials often leads to ordering or layering according to hard−soft acid−base (HSAB) theory, whereby the anionic species segregate as a result of preferential bonding to their corresponding hard or soft pair.[9,10] Heteroanionic materials often consist of homoleptic polyhedra, where only one type of an anion coordinates each cation, or heteroleptic polyhedra, where multiple types of an anion coordinate each cation. Heteroleptic bonding can occur when the metal cations are amphoteric (e.g., classified as borderline hard or soft Lewis acids), the anionic species are similar in size (e.g., N^{3-}, O^{2-}, S^{2-}, F^-), or the anions are sufficiently small that they can coordinate around the same metal cation. This, in turn, may generate irregularities in bonding, such as the lengths of metal−anion bonds, which influence local polarization and crystal fields.[1,11] On the whole, the long-range ordering of either of these bonding types yields global changes in the material properties.[2,11]

A particularly rich system for such exploration is that of the chalcogenides, which are well known due to the impressive structural and bonding diversity inherent to this class of materials.[12−16] Heteroanionic exploration of chalcogenides can harness these features, including the tendency for sulfur, selenium, and tellurium to catenate; so beyond introducing two different anions (such as S^{2-} and Se^{2-}), oligomerized anionic units can also be introduced.[13] In addition to discrete anions, chalcogenides have also presented as dumbbells,[17−23] chains,[14,16,24−28] rings,[21,29] nets or sheets,[15,21,30,31] propellers,[32] and cross-shaped units.[29]

Though limited to date, the synthesis of mixed chalcogenides has been demonstrated with the heteroanionic compounds crystallizing in either the same structure type as the parent compound or in a new structure type.[11,33] The differences in electronegativity and size are sufficient to produce compounds with anions on distinct crystallographic sites (as opposed to solid solutions or anion substitutions, where the anions are positionally disordered).[34,35] In fact, it has been observed that a 10% difference in anionic size stabilizes an ordered structure

Received: January 24, 2022
Published: June 3, 2022

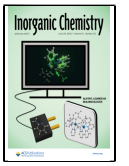

https://doi.org/10.1021/acs.inorgchem.2c00265
Inorg. Chem. 2022, 61, 9040−9046

instead of resulting in a solid solution.[11,36] It has also been suggested that the closer the Q:Q' ratio is to unity, the higher the dimensionality of the structure; for example, a 1:1 ratio often yields a three-dimensional (3D) lattice, 2:1 a two-dimensional (2D) lattice, and 6:1 a zero-dimensional (0D) lattice.[11] When the anions order, they may remain in the parent structure type or crystallize in a different structure type. Ibers and co-workers exchanged one sulfur for tellurium in $LnCuS_2$ (Ln = La, Sm).[25] The two sulfurs in the parent structure were on independent crystallographic sites. When Te was introduced, it fully substituted for S in both compounds and preferentially bonded to Cu following HSAB theory. The resulting compound LaCuSTe crystallized in the same parent structure type, but SmCuSTe crystallized in a different structure type. Crystallizing in the parent structure type is also seen when substituting in the compounds β-US_2 and β-USe_2.[37] More frequently, a new structure type forms.[11,33,38,39] Overall, there has been a limited exploration into main group elements, particularly for heteroanionic ternaries.

Herein, we describe the synthesis, structure, and properties of the indium heteroanion $In_8S_{2.82}Te_{6.18}(Te_2)_3$, which contains the three anions S^{2-}, Te^{2-}, and Te_2^{2-}. The In−S−Te phase space was inspired by the formation of the heteroanionic ternary Ga_2S_2Te, where the chemical similarity between gallium and indium showed promise in the formation of an indium ternary. In pursuit of this heteroanionic ternary, indium was used as it is borderline soft and therefore willing to bond with both S and Te according to HSAB theories. This material's identity as a narrow bandgap semiconductor of 1.12(2) eV and the presence of heavy elements suggest promise as a thermoelectric material. Its complex structure is expected to scatter phonons and minimize lattice thermal conductivity, which is also favorable for thermoelectric materials. Moreover, the potential tuning of the sulfur−tellurium mixed occupancy offers opportunities for future work.

EXPERIMENTAL SECTION

Chemicals. Indium metal (99.99%, American Elements), sulfur (sublimed, 99.99%, Spectrum), tellurium (99.99%, American Elements), and glassy carbon (99.9%, Aldrich) were used as obtained.

Synthesis. *Indium Sulfide, InS.* A 1.9542 g amount (17.02 mmol) of indium was combined with 0.5458 g (17.02 mmol) of elemental sulfur in a fused silica tube (9 mm OD), which was subsequently flame-sealed under vacuum (10^{-3} mbar). The sample was heated to 800 °C for 24 h, soaked at 800 °C for 24 h, and then air-quenched.

$In_8S_{2.82}Te_{6.18}(Te_2)_3$. A 0.3174 g amount (2.16 mmol) of synthesized InS was combined with 0.4826 g (3.78 mmol) of elemental tellurium in a fused silica tube (9 mm OD), which was subsequently flame-sealed under vacuum (10^{-3} mbar). The sample was heated to 500 °C for 6 h and soaked at 500 °C for 24 h, before furnace cooling for batch synthesis. Dark gray single crystals were prepared using the above procedure, but with a maximum temperature of 650 °C and slow cooling at 2.75 °C/min to 450 °C before furnace cooling to room temperature. The bulk phase pure material, which is air-stable, can be prepared using the reactions 3InS + 5InTe + 7Te as well as In_2S_3 + $3In_2Te_3$ + 3Te.

Physical Measurements. *Powder X-ray Diffraction.* A Rigaku Miniflex600 diffractometer, operated at 40 kV and 15 mA, was used to collect X-ray powder diffraction patterns. The diffractometer was equipped with Ni-filtered Cu Kα radiation (1.5406 Å) and a high-speed silicon strip detector. The diffraction patterns were collected using a scan rate of 10°/min and a scan width of 0.02°. The crystal structures were visualized with Vesta software.[40]

Single-Crystal X-ray Diffraction. Intensity data of a black rectangular single crystal of $In_8S_{2.82}Te_{6.18}(Te_2)_3$ was collected at 100(2) K. A suitable single crystal mounted on a glass fiber with glue was measured on an STOE StadiVari diffractometer, which was run at 65 kV and 0.68 mA and equipped with an AXO Ag Kα microfocus sealed X-ray A-MiXS source (λ = 0.560834 Å) as well as a Dectris Pilatus3 R CdTe 300 K Hybrid Photon Counting detector. An Oxford Cryosystems low-temperature device controlled the temperature of the crystal. Data reduction was performed with the X-Area software package using a numerical absorption correction. The structure was solved with the ShelXT structure solution program using direct methods and Olex2 as the graphical interface. The model was refined with ShelXL using least-squares minimization.

In Situ Powder X-ray Diffraction. Temperature-dependent data was collected on an STOE STADI MP high-resolution diffractometer with an oven attachment (STOE HT), operating at 40 kV and 40 mA. The diffractometer was equipped with Ag Kα1 radiation (λ = 0.559407 Å), a one-dimensional silicon strip detector (MYTHEN2 1K from DECTRIS), and an asymmetrically curved Germanium monochromator. The ternary sample was sieved (<45 μm) and diluted using glassy carbon to mitigate sample attenuation of the X-ray beam. The sample−carbon mixtures were then packed into 0.3 mm diameter quartz capillaries that were subsequently flame-sealed under vacuum (ca. 3.0 × 10^{-3} mbar). Prior to the measurement, the instrument was calibrated against a NIST Silicon standard (640 d). The diffraction data were collected at 25, 100, 150, 200, 250, 300, 350, 375, 400, 425, 450, 500, and 550 °C upon heating and the reverse upon cooling, with temperature stability typically at 0.1 °C. The heating rate was 10.0 °C/min and the collection range was 2−22° 2θ. Samples were spun throughout the collection.

Photoemission Yield Spectroscopy in Air (PYSA). Photoemission yield spectroscopy in air[41,42] (PYSA) was performed using an AC-2 Riken-Keiki instrument with a tunable monochromatic ultraviolet light source (4.2−6.2 eV). The measurements were performed under ambient conditions. Photoelectrons were generated when the photon energy is higher than the work function and those generated photoelectrons were measured at each excitation energy. The linear onset of the PYSA spectra results in the work function that is equal to the valence band maximum with respect to the vacuum energy for a semiconductor.

Scanning Electron Microscopy−Energy-Dispersive Spectroscopy. Micrographs were collected using a Hitachi S-3400 scanning electron microscope. Quantitative analysis was performed at 20 kV and used the attached PGT energy-dispersive X-ray analysis instrument.

Computational Methods. All density functional theory (DFT) calculations were performed using the Vienna ab initio simulation package (VASP)[43,44] along with the projector augmented wave (PAW)[45,46] method to perform the density functional theory (DFT) calculations. The Perdew−Burke−Ernzerhof (PBE)[47] generalized gradient approximation (GGA) was used as the exchange−correlation functional. The x = 0 structure $In_8S_3Te_{12}$ structure was constructed by letting the S/Te mixing sites be fully occupied by S atoms, resulting in an ordered 46-atom unit cell. The plane wave cutoff energy was set as 520 eV, the structure was fully relaxed until the total energy converged to within 10^{-8} eV, and the force on each atom was less than 10^{-3} eV/Å. We sampled the Brillouin zone using γ-centered k-point meshes of 6 × 6 × 5 for the unit cell $In_8S_3Te_{12}$. Phonon calculations were performed with the 1 × 1 × 1 unit cell using the PHONOPY package.[48] The transport properties were calculated using the semiclassical Boltzmann transport theory implemented in the BoltzTraP[49] package.

RESULTS AND DISCUSSION

$In_8S_{2.82}Te_{6.18}(Te_2)_3$ was discovered searching for the In-analogue to the mixed chalcogenide, Ga_2S_2Te. Our synthesis approach for Ga_2S_2Te used GaS and Te as starting materials. Therefore, the analogous binary InS was used to target In_2S_2Te. By systematically increasing the amount of tellurium present in the reaction, $In_8S_{2.82}Te_{6.18}(Te_2)_3$ was discovered. Black single crystals were grown after making a bulk phase pure batch and running thermal analysis (Figure S1), which allowed for an optimal heating profile to be used.

https://doi.org/10.1021/acs.inorgchem.2c00265
Inorg. Chem. 2022, 61, 9040−9046

Single-crystal X-ray diffraction reveals that $In_8S_{2.82}Te_{6.18}(Te_2)_3$ crystallizes in the monoclinic space group $C2/c$, with lattice parameters given in Table 1 and atomic coordinates, anisotropic displacement parameters, bond lengths, and bond angles shown in Tables S1−S4. SEM-EDS measurements validated the composition determined in the single-crystal diffraction and yielded In:S:Te ratios of 8:3:12 (Table S5). The structure of $In_8S_{2.82}Te_{6.18}(Te_2)_3$ is a complex 3D network of corner-connected InQ_4 tetrahedra with three Te_2^{2-} dumbbell dimers per formula unit, as shown in Figure 1. There are four distinct tetrahedral sites, each of which has three Te vertices and one S vertex, and these tetrahedra are corner-connected to neighboring tetrahedra as well as bridged by Te_2^{2-}.

Within each Te_2^{2-} dimer, one tellurium is a crystallographically distinct tellurium atom and the Te−Te bond lengths are 2.9244(8) Å, 2.8928(8) Å, and 2.9024(7) Å for Te4, Te5, and Te6, respectively. These lengths are similar to those of previous examples of compounds with only Te−Te dimers (2.70−2.86 Å)[14,21] as well as with a mixture of individual tellurium anions and chains (2.74−2.82 Å).[22,23] The local coordination environment of each Te_2^{2-} dimer is unusual and is shown in Figure 2a−c. Each Te atom of the Te_2^{2-} dimer is three-coordinate and covalently bonded to two In atoms and the other Te atom is comprising its dimer. Each of the three dimers has different local coordination environments because of their bonding to distinct sets of In-centered tetrahedra.

The four distinct tetrahedral indium atom environments are shown in Figure 2d−g. Each environment contains a Te^{2-} anion and a Te_2^{2-} dimer, while differing in having a fully or primarily sulfur site and a second Te^{2-} anion or Te_2^{2-} dimer. The indium tetrahedra In1, In2, and In3 contain a full sulfur (S1), which links the three indium tetrahedra and thereby has a three-fold coordination environment. Meanwhile, In4 includes a mixed occupancy sulfur−tellurium site (S2/Te7) that was refined to be 81.9(5)% sulfur and 18.1(5)% tellurium and bridges the two neighboring In4 tetrahedra. As a result, this disordered S/Te site has a two-fold coordination environment. The bond length of this four-coordinate indium and disordered chalcogenide is 2.5409(10) Å and, as expected, more closely aligns with that of four-coordinate indium and sulfur in In_xS_y binaries (2.427(9)−2.5379(12) Å)[50−52] than that of four-coordinate indium and tellurium in In_xTe_y binaries (2.6624(5)−2.921(7) Å).[53−55] For their remaining anion, In1 and In4 have a second Te_2^{2-} dimer, while In2 and In3 have a second Te^{2-} anion.

As viewed down the c-axis, the In1 and In3 tetrahedra form infinite chains down the c-axis surrounding the Te4 dimer and

Table 1. Crystal Data and Structure Refinement for $In_8S_{2.82}Te_{12.18}$ at 100 K[a]

empirical formula	$In_8S_{2.82}Te_{12.18}$
formula weight	2563.38
temperature	100 K
wavelength	0.56083 Å
crystal system	monoclinic
space group	$C2/c$
unit cell dimensions	a = 14.2940(6) Å, α = 90°
	b = 14.3092(4) Å, β = 90.845(3)°
	c = 14.1552(6) Å, γ = 90°
volume	2894.93(19) Å^3
Z	1
density (calculated)	5.881 g/cm^3
absorption coefficient	9.605 mm^{-1}
F(000)	4282
θ range for data collection	2.246−27.863°
index ranges	$-21 \le h \le 21$, $-21 \le k \le 21$, $-21 \le l \le 21$
reflections collected	80 350
independent reflections	5481 [R_{int} = 0.0872]
completeness to θ = 19.664°	99.9%
refinement method	full-matrix least squares on F^2
data/restraints/parameters	5481:0:106
goodness-of-fit	1.041
final R indices [$I > 2\sigma(I)$]	R_{obs} = 0.0377, wR_{obs} = 0.0958
R indices [all data]	R_{all} = 0.0433, wR_{all} = 0.1000
largest diff. peak and hole	2.900 and −3.603 e·Å^{-3}

[a] $R = \sum||F_o| - |F_c||/\sum|F_o|$, $wR = \{\sum[w(|F_o|^2 - |F_c|^2)^2]/\sum[w(|F_o|^4)]\}^{1/2}$ and $w = 1/[\sigma^2(F_o^2) + (0.0660P)^2 + 18.3583P]$ where $P = (F_o^2 + 2F_c^2)/3$.

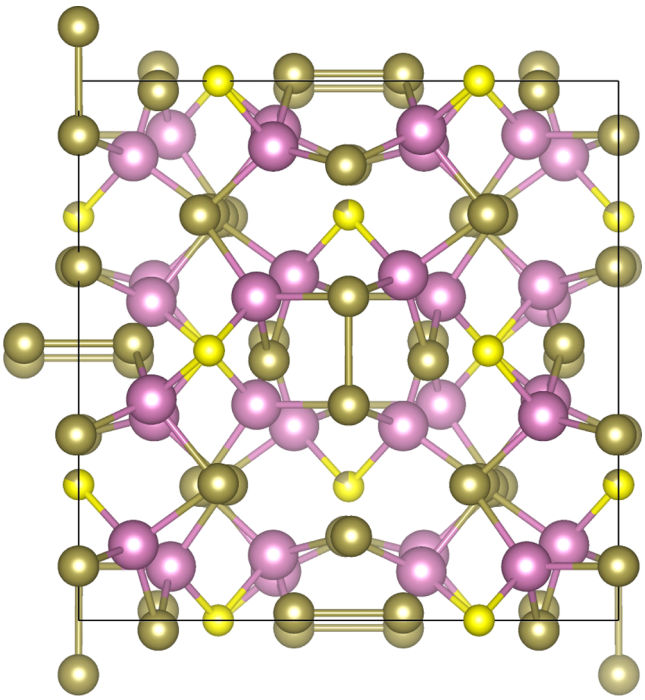

Figure 1. Crystal structure of $In_8S_{2.82}Te_{6.18}(Te_2)_3$ viewed down the c-axis. Purple spheres are indium, yellow sulfur, and brown tellurium.

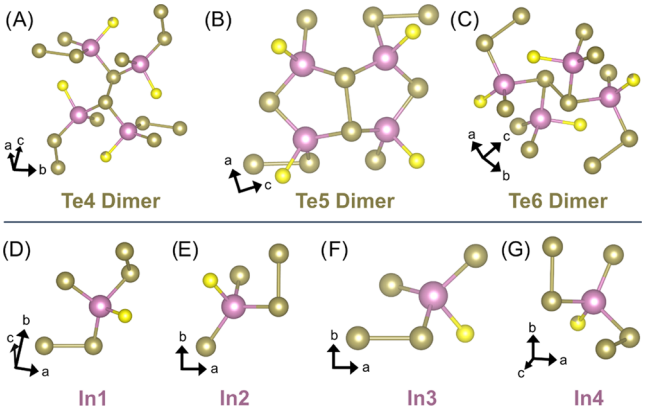

Figure 2. Local coordination environment for the three crystallographically distinct Te_2^{2-}: (A) Te4, (B) Te5, and (C) Te6 and the local coordination environments for the four crystallographically distinct. In sites: (D) In1, (E) In2, (F) In3, and (G) In4. The entire Te_2^{2-} dimers are shown in all coordination environments. Purple spheres are indium, yellow sulfur, and brown tellurium.

https://doi.org/10.1021/acs.inorgchem.2c00265
Inorg. Chem. 2022, 61, 9040−9046

are tilted in phase with each other in mirror-like symmetry (Figures 3 and 4). In contrast, the In2 and In4 tetrahedra form similar chains corner-connected to the Te6 dimer; however, the In4 tetrahedra tilt out of phase with In2 and the other two tetrahedra, forcing the bridging S2/Te7 site out of the a−b plane of the S1 atoms shared by In1, In2, and In3.

The calculated electronic band structure of $In_8S_{2.82}Te_{6.18}(Te_2)_3$ is shown in Figure 5a. This heteroanionic material is an indirect bandgap semiconductor with a calculated bandgap of 0.99 eV. This is consistent with the experimental bandgap of 1.12(2) eV (1107 nm, Figure 5b). The work function was measured using photoemission yield spectroscopy in air[41,42] and found to be 5.15(5) eV (241 nm, Figure 5c). Using the experimental bandgap and valence band maximum (VBM), the conduction band minimum (CBM) is calculated to be at 4.03(5) eV.

The CBM is at the Γ point of the Brillouin zone, while the VBM can be found along the A−I_2 direction. The conduction bands near the Fermi level are mainly contributed by Te 5p and In 5s orbits, while the valence bands near the Fermi level are mainly contributed by Te 5p and S 3p orbits. In $In_8S_{2.82}Te_{6.18}(Te_2)_3$, sulfur acts as a structural templating agent but does not significantly affect the electronic behavior, as the S states lie nearly 1 eV below the VBM. Overall, the top of the valence band is more dispersive than the bottom of the conduction band, which is due to the dominated contribution of Te 5p orbitals localized at the top of the valence band, as shown in Figure 5a. Thus, the charge transport of holes would be more efficient than that of electrons. This is supported by the electron effective mass calculations of 0.554 and 0.668 (in m_0) for the directions $\Gamma - L_2$ and $\Gamma - V_2$, respectively; meanwhile, the hole effective mass is calculated to be 0.411 and 0.208 for the directions $L_2 - \Gamma$ and $V_2 - \Gamma$, respectively.

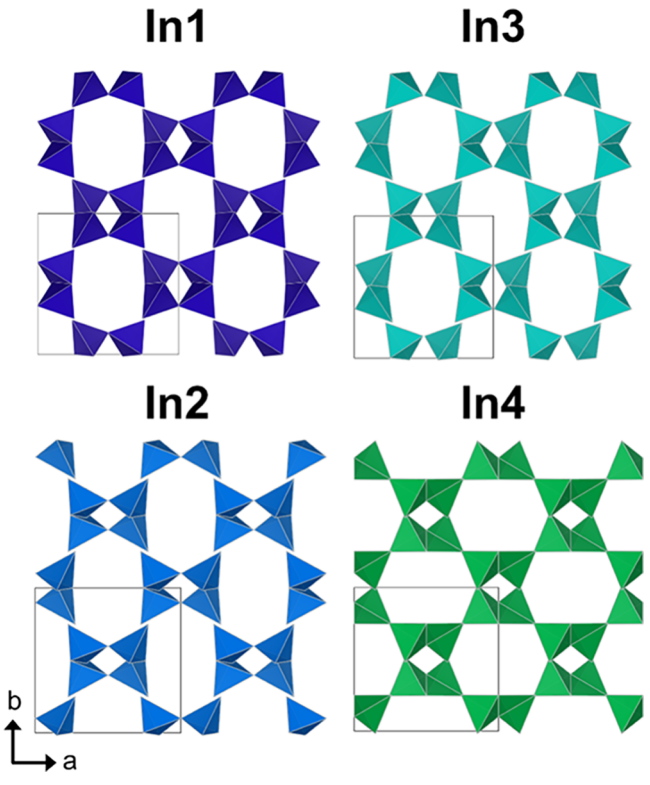

Figure 3. Tetrahedral 3D network of InQ_4, viewed down the *c*-axis. Each indium tetrahedron is shown individually to highlight its arrangement in the crystal structure. Only the In4 tetrahedra connect to themselves via corner-sharing of their one mixed sulfur and tellurium site, S2/Te7.

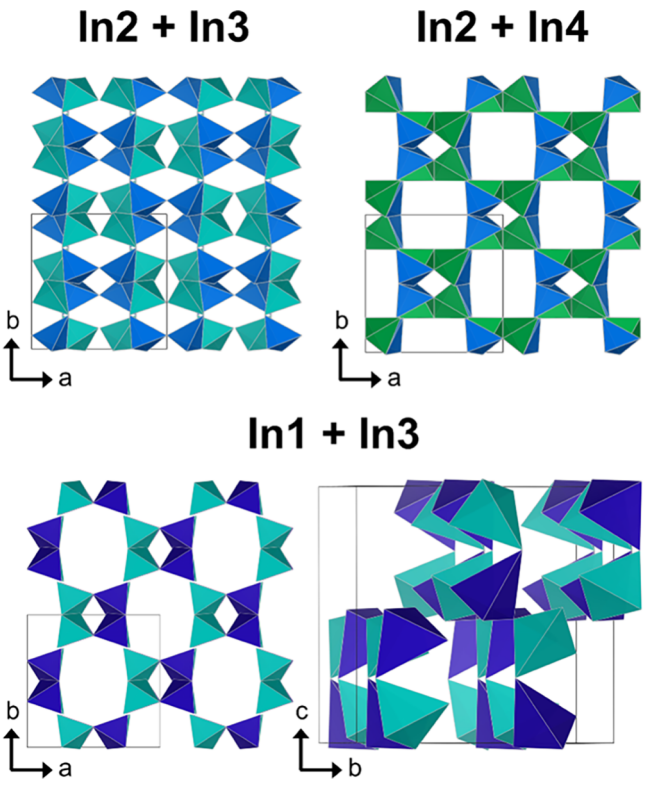

Figure 4. Connectivity of indium tetrahedra in $In_8S_{2.82}Te_{6.18}(Te_2)_3$. In2 and In3 are connected via corner-sharing of S1 and Te1. In2 and In4 are connected via corner-sharing of S2/Te7, Te3, and Te6. In1 and In3 are connected via corner-sharing of S1, Te2, and Te5 into chains parallel to the *c*-axis. Shown tilted down the *a*-axis to show the tetrahedra connectivity.

As this material is a relatively narrow bandgap semiconductor, incorporates several heavy elements, and has multiple energy converged bands near the VBM, it shows potential as a thermoelectric material. Moreover, the complicated crystal structure of this material is expected to scatter phonons and minimize lattice thermal conductivity. Therefore, we conducted Seebeck (S), electrical conductivity (σ), and power factor ($S^2\sigma$) calculations, and the results are shown in Figure 6. (The thermal conductivity could not be calculated as the ordered structure used for this calculation has imaginary phonon modes, as shown in Figure S3.) The calculated electrical conductivity (as shown in Figure 6) aligns with the argument that the electrical conductivity is higher for holes than for electrons. By fixing the relaxation time to 10 fs, our predictions suggest that the power factor along the *yy* direction for hole carriers can be over 30 μW/(cm K^2) at 300 K. $In_8S_{2.82}Te_{6.18}(Te_2)_3$ shows promise as a p-type thermoelectric, with a potential power factor similar to that of bulk n-type Bi_2Te_3 at 300 K.[56]

CONCLUSIONS

This heteroanionic ternary $In_8S_{3-x}Te_{6+x}(Te_2)_3$ (x = 0.18) features a novel structure in that it comprises three different anions: S^{2-}, Te^{2-}, and Te_2^{2-}. While the initial target In_2S_2Te was not observed, a new complex 3D framework of $In_8S_{3-x}Te_{6+x}(Te_2)_3$ (x = 0.18) was discovered consisting of corner-sharing InQ_4 tetrahedra and Te_2^{2-} dumbbell dimers.

https://doi.org/10.1021/acs.inorgchem.2c00265
Inorg. Chem. 2022, 61, 9040−9046

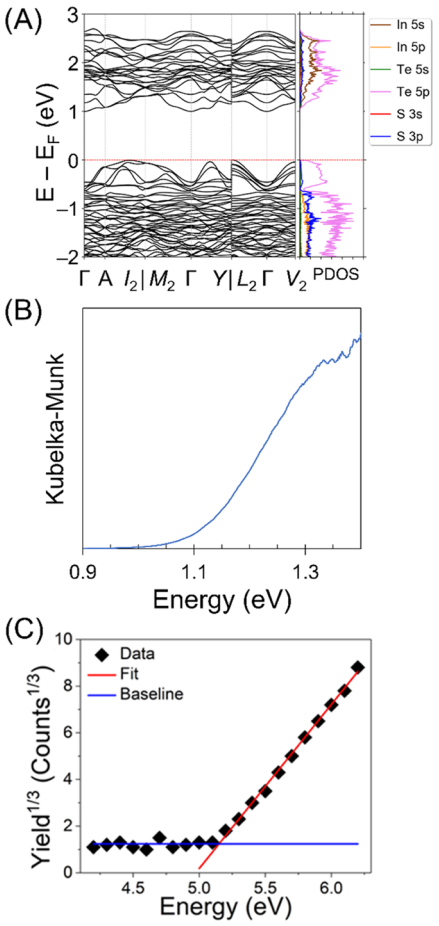

Figure 5. (A) Calculated band structure and partial density of states (PDOS) of $In_8S_3Te_{12}$. (B) Experimental bandgap of 1.12(2) eV for $In_8S_{2.82}Te_{6.18}(Te_2)_3$. (C) Experimental work function of 5.15(5) eV.

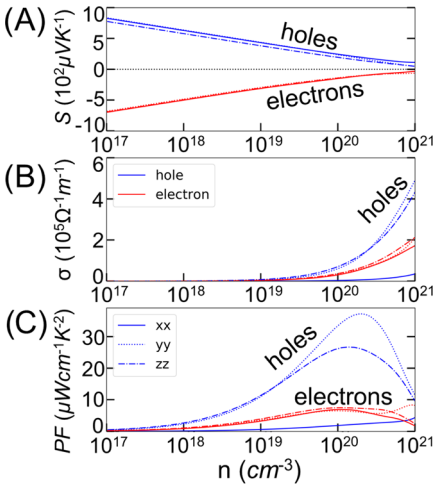

Figure 6. Calculated electrical transport properties of $In_8S_3Te_{12}$ including (A) Seebeck coefficient, (B) electrical conductivity, and (C) power factor calculated at 300 K with relaxation time fixed at 10 fs. Blue lines and red lines are holes and electrons, respectively.

Future work should explore hole doping as the presence of heavy atoms in its complicated structure in conjunction with its predicted physical and electrical properties and the multiband nature of the valence band indicates promise as a p-type thermoelectric material.

■ ASSOCIATED CONTENT

Supporting Information

The Supporting Information is available free of charge at https://pubs.acs.org/doi/10.1021/acs.inorgchem.2c00265.

Experimental details on optical measurements and differential thermal analysis, crystallographic tables (PDF)

Accession Codes

CCDC 2144207 contains the supplementary crystallographic data for this paper. These data can be obtained free of charge via www.ccdc.cam.ac.uk/data_request/cif, or by emailing data_request@ccdc.cam.ac.uk, or by contacting The Cambridge Crystallographic Data Centre, 12 Union Road, Cambridge CB2 1EZ, UK; fax: +44 1223 336033.

■ AUTHOR INFORMATION

Corresponding Author

Mercouri G. Kanatzidis − *Department of Chemistry, Northwestern University, Chicago, Illinois 60208, United States;* orcid.org/0000-0003-2037-4168; Email: m-kanatzidis@northwestern.edu

Authors

Rebecca McClain − *Department of Chemistry, Northwestern University, Chicago, Illinois 60208, United States;* orcid.org/0000-0002-1906-9791

Craig C. Laing − *Department of Chemistry, Northwestern University, Chicago, Illinois 60208, United States;* orcid.org/0000-0002-0654-4741

Jiahong Shen − *Department of Materials Science and Engineering, Northwestern University, Chicago, Illinois 60208, United States;* orcid.org/0000-0002-1951-2183

Christopher Wolverton − *Department of Materials Science and Engineering, Northwestern University, Chicago, Illinois 60208, United States;* orcid.org/0000-0003-2248-474X

Complete contact information is available at: https://pubs.acs.org/10.1021/acs.inorgchem.2c00265

Notes

The authors declare no competing financial interest.

■ ACKNOWLEDGMENTS

This work (RM) was supported in part by the National Science Foundation through the MRSEC program (NSF-DMR 1720139). The work was funded in part (CCL) by NSF (grant DMR- 2003476). The authors thank KMM for helpful discussions. This work made use of the IMSERC Crystallography facility at Northwestern University, which has received support from the Soft and Hybrid Nanotechnology Experimental (SHyNE) Resource (NSF ECCS-2025633), and Northwestern University. Purchase of the Ag-microsource diffractometer used to obtain results included in this publication was supported by the Major Research Instrumentation Program from the National Science Foundation under the award CHE-1920248.

■ REFERENCES

(1) Kageyama, H.; Hayashi, K.; Maeda, K.; Attfield, J. P.; Hiroi, Z.; Rondinelli, J. M.; Poeppelmeier, K. R. Expanding frontiers in materials chemistry and physics with multiple anions. *Nat. Commun.* **2018**, *9*, No. 772.

(2) Harada, J. K.; Charles, N.; Poeppelmeier, K. R.; Rondinelli, J. M. Heteroanionic Materials by Design: Progress Toward Targeted Properties. *Adv. Mater.* **2019**, *31*, No. 1805295.
(3) Pan, Y.; Guo, S.-P.; Liu, B.-W.; Xue, H.-G.; Guo, G.-C. Second-order nonlinear optical crystals with mixed anions. *Coord. Chem. Rev.* **2018**, *374*, 464−496.
(4) Oba, F.; Kumagai, Y. Design and exploration of semiconductors from first principles: A review of recent advances. *Appl. Phys. Express* **2018**, *11*, No. 060101.
(5) Park, G. D.; Park, J.-S.; Kim, J. K.; Kang, Y. C. Recent Advances in Heterostructured Anode Materials with Multiple Anions for Advanced Alkali-Ion Batteries. *Adv. Energy Mater.* **2021**, *11*, No. 2003058.
(6) Li, Y.-Y.; Wang, W.-J.; Wang, H.; Lin, H.; Wu, L.-M. Mixed-Anion Inorganic Compounds: A Favorable Candidate for Infrared Nonlinear Optical Materials. *Cryst. Growth Des.* **2019**, *19*, 4172−4192.
(7) Kubo, A.; Giorgi, G.; Yamashita, K. Anion Ordering in CaTaO2N: Structural Impact on the Photocatalytic Activity. Insights from First-Principles. *Chem. Mater.* **2017**, *29*, 539−545.
(8) Besara, T.; Ramirez, D.; Sun, J.; Whalen, J. B.; Tokumoto, T. D.; McGill, S. A.; Singh, D. J.; Siegrist, T. Ba2TeO: A new layered oxytelluride. *J. Solid State Chem.* **2015**, *222*, 60−65.
(9) Guittard, M.; Benazeth, S.; Dugué, J.; Jaulmes, S.; Palazzi, M.; Laruelle, P.; Flahaut, J. Oxysulfides and oxyselenides in sheets, formed by a rare earth element and a second metal. *J. Solid State Chem.* **1984**, *51*, 227−238.
(10) Clarke, S. J.; Adamson, P.; Herkelrath, S. J. C.; Rutt, O. J.; Parker, D. R.; Pitcher, M. J.; Smura, C. F. Structures, Physical Properties, and Chemistry of Layered Oxychalcogenides and Oxypnictides. *Inorg. Chem.* **2008**, *47*, 8473−8486.
(11) Valldor, M. Anion Ordering in Bichalcogenides. *Inorganics* **2016**, *4*, No. 23.
(12) Kanatzidis, M. G. Molten alkali-metal polychalcogenides as reagents and solvents for the synthesis of new chalcogenide materials. *Chem. Mater.* **1990**, *2*, 353−363.
(13) Kanatzidis, M. G.; Huang, S.-P. Coordination chemistry of heavy polychalcogenide ligands. *Coord. Chem. Rev.* **1994**, *130*, 509−621.
(14) Smith, D. M.; Ibers, J. A. Syntheses and solid-state structural chemistry of polytelluride anions. *Coord. Chem. Rev.* **2000**, *200*−*202*, 187−205.
(15) Sheldrick, W. S. Polychalcogenide Anions: Structural Diversity and Ligand Versatility. *Z. Anorg. Allg. Chem.* **2012**, *638*, 2401−2424.
(16) Kanatzidis, M. G. Discovery-Synthesis, Design, and Prediction of Chalcogenide Phases. *Inorg. Chem.* **2017**, *56*, 3158−3173.
(17) Furuseth, S.; Brattas, L.; Kjekshus, A. Crystal Structure of HfTe 5. *Acta Chem. Scand.* **1973**, *27*, 2367−2374.
(18) Lowhorn, N. D.; Tritt, T. M.; Abbott, E. E.; Kolis, J. W. Enhancement of the power factor of the transition metal pentatelluride HfTe5 by rare-earth doping. *Appl. Phys. Lett.* **2006**, *88*, No. 022101.
(19) Miller, S. A.; Witting, I.; Aydemir, U.; Peng, L.; Rettie, A. J. E.; Gorai, P.; Chung, D. Y.; Kanatzidis, M. G.; Grayson, M.; Stevanović, V.; Toberer, E. S.; Snyder, G. J. Polycrystalline $ZrTe_5$ Parametrized as a Narrow-Band-Gap Semiconductor for Thermoelectric Performance. *Phys. Rev. Appl.* **2018**, *9*, No. 014025.
(20) Chen, X.; Huang, X.; Li, J. Rb4Hg5(Te2)2(Te3)2Te3, [Zn(en)3]4In16(Te2)4(Te3)Te22, and K2Cu2(Te2)(Te3): Novel Metal Polytellurides with Unusual Metal−Tellurium Coordination. *Inorg. Chem.* **2001**, *40*, 1341−1346.
(21) Böttcher, P. Tellurium-Rich Tellurides. *Angew. Chem., Int. Ed. Engl.* **1988**, *27*, 759−772.
(22) Canadell, E.; Jobic, S.; Brec, R.; Rouxel, J. Electronic structure and properties of anionic mixed valence and layered CrTe3: The question of extended tellurium bonding in transition metal tellurides. *J. Solid State Chem.* **1992**, *98*, 59−70.
(23) Mar, A.; Ibers, J. A. The layered ternary germanium tellurides ZrGeTe4, HfGeTe4, and TiGeTe6: structure, bonding, and physical properties. *J. Am. Chem. Soc.* **1993**, *115*, 3227−3238.
(24) Fenske, D.; Baum, G.; Wolkers, H.; Schreiner, B.; Weller, F.; Dehnicke, K. Die Kristallstrukturen der Polytelluride [Ca(DMF)6]-Te4, [Sr(15-Krone-5)2]Te4 · H2O, {[BaCl(18-Krone-6)(DMF)2]2-[BaCl(18-Krone-6)(DMF) (H2O)]2(Te4)2} und [Ph3PNPPh3]-2Te5 · 2 DMF. *Z. Anorg. Allg. Chem.* **1993**, *619*, 489−499.
(25) Huang, F. Q.; Ibers, J. A. Syntheses, Structures, and Theoretical Study of LaCuSTe and SmCuSTe. *Inorg. Chem.* **1999**, *38*, 5978−5983.
(26) Maier, S.; Ohno, S.; Yu, G.; Kang, S. D.; Chasapis, T. C.; Ha, V. A.; Miller, S. A.; Berthebaud, D.; Kanatzidis, M. G.; Rignanese, G. M.; Hautier, G.; Snyder, G. J.; Gascoin, F. Resonant Bonding, Multiband Thermoelectric Transport, and Native Defects in n-Type BaBiTe3−xSex (x = 0, 0.05, and 0.1). *Chem. Mater.* **2018**, *30*, 174−184.
(27) Chung, D.-Y.; Jobic, S.; Hogan, T.; Kannewurf, C. R.; Brec, R.; Rouxel, J.; Kanatzidis, M. G. Oligomerization Versus Polymerization of Texn- in the Polytelluride Compound BaBiTe3. Structural Characterization, Electronic Structure, and Thermoelectric Properties. *J. Am. Chem. Soc.* **1997**, *119*, 2505−2515.
(28) Assoud, A.; Derakhshan, S.; Soheilnia, N.; Kleinke, H. Electronic Structure and Physical Properties of the Semiconducting Polytelluride Ba2SnTe5 with a Unique Te54- Unit. *Chem. Mater.* **2004**, *16*, 4193−4198.
(29) Zhang, Q.; Malliakas, C. D.; Kanatzidis, M. G. {[Ga(en)3]2-(Ge2Te15)}n: A Polymeric Semiconducting Polytelluride with Boat-Shaped Te84− Rings and Cross-Shaped Te56− Units. *Inorg. Chem.* **2009**, *48*, 10910−10912.
(30) Patschke, R.; Kanatzidis, M. G. Polytelluride compounds containing distorted nets of tellurium. *Phys. Chem. Chem. Phys.* **2002**, *4*, 3266−3281.
(31) Zhang, X.; Li, J.; Foran, B.; Lee, S.; Guo, H.-Y.; Hogan, T.; Kannewurf, C. R.; Kanatzidis, M. G. Distorted Square Nets of Tellurium in the Novel Quaternary Polytelluride K0.33Ba0.67AgTe2. *J. Am. Chem. Soc.* **1995**, *117*, 10513−10520.
(32) Assoud, A.; Kleinke, H. A Polyselenide with a Novel Se78− Unit: the Structure of Sr19−xPbxGe11Se44 with x = 5.0 and 6.4. *Eur. J. Inorg. Chem.* **2017**, *2017*, 5515−5520.
(33) Mayasree, O.; Sankar, C. R.; Assoud, A.; Kleinke, H. New Barium Copper Chalcogenides Synthesized Using Two Different Chalcogen Atoms: Ba2Cu6−xSTe4 and Ba2Cu6−xSeyTe5−y. *Inorg. Chem.* **2011**, *50*, 4580−4585.
(34) Zhang, X.; Kanatzidis, M. G. AMTeS3 (A = K, Rb, Cs; M = Cu, Ag): A New Class of Compounds Based on a New Polychalcogenide Anion, TeS32. *J. Am. Chem. Soc.* **1994**, *116*, 1890−1898.
(35) Schleid, T.; Klein, E. K. Nd2S2Te: Neodymium(III) Sulfide Telluride with Ce2O2S-Type Crystal Structure. *Z. Anorg. Allg. Chem.* **2001**, *627*, 807−808.
(36) Hume-Rothery, W.; Powell, H. M. On the Theory of Super-Lattice Structures in Alloys. *Z. Kristallogr. - Cryst. Mater.* **1935**, *91*, 23−47.
(37) Troć, R.; Kaczorowski, D.; Shlyk, L.; Potel, M.; Noël, H. Crystal structure, magnetic and electrical transport studies of single crystals of the uranium mixed chalcogenides: USSe, USte and USeTe. *J. Phys. Chem. Solids* **1994**, *55*, 815−823.
(38) Luo, Z.-Z.; Lin, C.-S.; Cheng, W.-D.; Yang, Y.; Li, Y.-B.; Zhang, H.; Zhang, W.-L.; He, Z.-Z. Syntheses, crystal and electronic structures, and characterizations of the mixed anions compounds Ba4In2Te2Q5 (Q = S, Se). *CrystEngComm* **2013**, *15*, 4773−4778.
(39) Hodges, J. M.; Xia, Y.; Malliakas, C. D.; Alexander, G. C. B.; Chan, M. K. Y.; Kanatzidis, M. G. Two-Dimensional CsAg5Te3−xSx Semiconductors: Multi-anion Chalcogenides with Dynamic Disorder and Ultralow Thermal Conductivity. *Chem. Mater.* **2018**, *30*, 7245−7254.
(40) Momma, K.; Izumi, F. VESTA: a three-dimensional visualization system for electronic and structural analysis. *J. Appl. Crystallogr.* **2008**, *41*, 653−658.
(41) Yamashita, D.; Ishizaki, A. In situ measurements of change in work function of Pt, Pd and Au surfaces during desorption of oxygen by using photoemission yield spectrometer in air. *Appl. Surf. Sci.* **2016**, *363*, 240−244.
(42) Harwell, J. R.; Baikie, T. K.; Baikie, I. D.; Payne, J. L.; Ni, C.; Irvine, J. T. S.; Turnbull, G. A.; Samuel, I. D. W. Probing the energy levels of perovskite solar cells via Kelvin probe and UV ambient

https://doi.org/10.1021/acs.inorgchem.2c00265
Inorg. Chem. 2022, 61, 9040−9046

pressure photoemission spectroscopy. *Phys. Chem. Chem. Phys.* **2016**, *18*, 19738−19745.
(43) Kresse, G.; Furthmüller, J. Efficient iterative schemes for ab initio total-energy calculations using a plane-wave basis set. *Phys. Rev. B: Condens. Matter Mater. Phys.* **1996**, *54*, 11169−11186.
(44) Kresse, G.; Furthmüller, J. Efficiency of ab-initio total energy calculations for metals and semiconductors using a plane-wave basis set. *Comput. Mater. Sci.* **1996**, *6*, 15−50.
(45) Blöchl, P. E. Projector augmented-wave method. *Phys. Rev. B: Condens. Matter Mater. Phys.* **1994**, *50*, 17953.
(46) Kresse, G.; Joubert, D. From ultrasoft pseudopotentials to the projector augmented-wave method. *Phys. Rev. B: Condens. Matter Mater. Phys.* **1999**, *59*, 1758.
(47) Perdew, J. P.; Burke, K.; Ernzerhof, M. Generalized gradient approximation made simple. *Phys. Rev. Lett.* **1996**, *77*, 3865.
(48) Togo, A.; Tanaka, I. First principles phonon calculations in materials science. *Scr. Mater.* **2015**, *108*, 1−5.
(49) Madsen, G. K.; Singh, D. J. BoltzTraP. A code for calculating band-structure dependent quantities. *Comput. Phys. Commun.* **2006**, *175*, 67−71.
(50) Adenis, C.; J, O. F.; Jumas, J. C.; Philippot, E. Etude structurale par spectroscopie Moessbauer et rayons X de spinelles lacunaires de type In2 S3. *Rev. Chim. Miner.* **1987**, *24*, 10−21.
(51) Rampersadh, N. S.; Venter, A. M.; Billing, D. G. Rietveld refinement of In2S3 using neutron and X-ray powder diffraction data. *Phys. B* **2004**, *350*, E383−E385.
(52) Bodnar, I. V.; K, A. G.; Korzun, B. V.; Smirnova, G. F. Preparation and properties of the compounds beta-In2S3, AgIn5S8, and CuIn5S8. *Inorg. Mater. (Transl. of Neorg. Mater.)* **1981**, *17*, 152−155.
(53) Woolley, J. C.; Pamplin, B. R.; Holmes, P. J. The ordered crystal structure of In2Te3. *J. Less-Common Met.* **1959**, *1*, 362−376.
(54) Sutherland, H. H.; Hogg, J. H. C.; Walton, P. D. Indium polytelluride In2Te5. *Acta Crystallographica Section B* **1976**, *32*, 2539−2541.
(55) Walton, P. D.; Sutherland, H. H.; Hogg, J. H. C. Indium polytelluride In2Te5(II). *Acta Crystallogr., Sect. B* **1978**, *34*, 41−45.
(56) Hong, M.; Chen, Z.-G.; Zou, J. Fundamental and progress of Bi2Te3-based thermoelectric materials. *Chin. Phys. B* **2018**, *27*, No. 048403.

https://doi.org/10.1021/acs.inorgchem.2c00265
Inorg. Chem. 2022, 61, 9040−9046